J. Fluid Mech. (2024), *vol*. 1000, A77, doi:10.1017/jfm.2024.1091

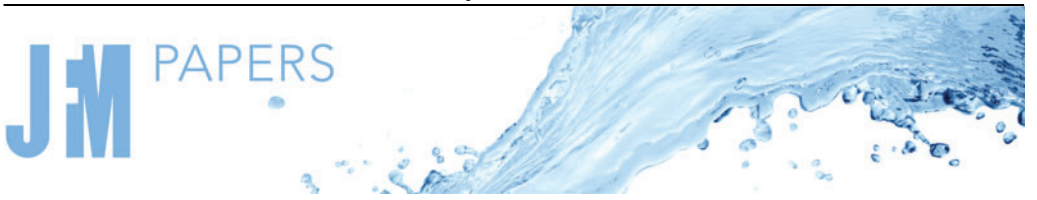

Suppressing capillary instability in falling liquid threads

Chase T. Gabbard[1], **James T. Rhoads**[2] **and Joshua B. Bostwick**[2],†

[1]School of Engineering, Brown University, Providence, RI 02912, USA

[2]Department of Mechanical Engineering, Clemson University, Clemson, SC 29631, USA

(Received 4 August 2024; revised 4 November 2024; accepted 10 November 2024)

A cylindrical liquid thread readily destabilizes into a series of drops due to capillary instability, which is also responsible for undesirable bead-on-fibre structures observed when coating a thin fibre. In this experimental study, we show how a falling liquid thread can be stabilized by internally distorting the cross-sectional shape using two vertically hung fibres. Below a critical flow rate Q_c, the dual-fibre system deforms the falling thread into a smooth column with a non-circular cross-section, thereby suppressing instability. Above Q_c, the cylindrical thread is left undeformed by the fibres and destabilizes into beads connected by a stable, non-cylindrical film. An empirical stability threshold is identified showing that flow delays the onset of capillary instability when compared with a marginally stable quasi-static coating. When the flow is unstable $Q > Q_c$, the bead velocity v obeys a simple scaling law that is well supported by our experiments over a large parameter range. This suppression technique can be extended to other slender geometries, such as a ribbon, which shows similar qualitative results but exhibits a different stability threshold due to spontaneous dewetting about its short edge.

Key words: capillary flows, thin films, instability control

1. Introduction

A falling liquid thread readily destabilizes into drops, as commonly observed in liquid falling from a kitchen faucet. Plateau (1873) attributed this instability to surface tension σ and found that drop formation was energetically more favourable than maintaining a uniform column of liquid. Rayleigh (1878) later considered inertia in a dynamic stability analysis and accurately predicted the critical cylinder length for destabilization, $l > (3\pi/2)^{1/3} r_0 \approx 1.67 r_0$, where r_0 is the cylinder radius. When coating a cylindrical

† Email address for correspondence: jbostwi@clemson.edu

object, the Plateau–Rayleigh instability manifests as liquid beads (Quéré 1999) or plugs (Camassa, Ogrosky & Olander 2014), depending on whether the coating is applied to the exterior or interior of the cylinder, respectively. In this paper, we introduce a technique for suppressing axial distortions in a falling liquid thread by mechanically deforming its cross-sectional shape using vertically hung parallel fibres, exploiting the fundamental differences in the stability of circular and non-circular threads.

The physics of capillary instability has been extensively studied, specifically the canonical formulation which considers the destabilization of a thread of viscosity μ, density ρ and radius r_0. Starting from the depth-averaged slender jet equations (Eggers & Dupont 1994), the most unstable wavenumber is $k_{max} = \sqrt{2}/(2r_0)$ in the inviscid limit $Oh = \mu/\sqrt{\rho\gamma r_0} << 1$ but $k_{max} \to 0$ in the viscous limit $Oh >> 1$ (Gallaire & Brun 2017) where Oh is the Ohnesorge number. Inertia is critical in setting the most unstable mode – thereby selecting the observed wavelength – while viscosity damps the growth rate of all unstable modes. These physics are similar to the capillary instability of liquid flowing down a fibre (Kliakhandler, Davis & Bankoff 2001), a well-studied variation of the classic Plateau–Rayleigh instability. Here, destabilization results in a bead-on-fibre structure rather than drop formation due to a no-penetration condition at the fluid–fibre interface. Frenkel (1992) derived a weakly nonlinear model for the thickness h of thin film flow down a fibre and showed that surface tension has both a stabilizing and destabilizing role due to the axial and azimuthal curvature of the interface, respectively. However, the capillary pressure is primarily influenced by azimuthal curvature, driving the instability and underscoring the relevance of the long-wavelength approximation often used to model these flows (Kalliadasis & Chang 1994; Chang & Demekhin 1999; Craster & Matar 2006; Ruyer-Quil *et al.* 2008).

Unlike a drop formed from a free jet, a liquid bead on a fibre has a relative amplitude that depends on the fibre radius r and can become small for large r, as demonstrated in figure 1(*a*) for silicone oil coating fibres of increasing radius. Although this reduces axial fluctuations in the coating, the beads can become asymmetric if the fibre radius is further increased (Gabbard & Bostwick 2021), the fluid is highly shear thinning (Gabbard & Bostwick 2023*a*) or the nozzle–fibre alignment is eccentric and Oh is large (Eghbali *et al.* 2022), leading to axial and azimuthal fluctuations, as shown in figure 1(*b*). Since the film between beads naturally adopts a cylindrical shape, the instability manifests whenever the characteristic bead period $\tau_{bead} > \tau_{PR}$, where $\tau_{PR} = 3\mu r^4/\sigma h^3$ is the typical time scale for the Plateau–Rayleigh instability for thin film flow on a fibre (Gallaire & Brun 2017). Figure 1(*c*) shows an example of multi-scale breakup where the thin film between primary beads destabilizes into secondary beads that can form 'dry spots' where only a microscopic liquid film persists. The liquid may also be externally perturbed to induce and remove beads from a smooth coating, e.g. using cross-flow (Cazaubiel & Carlson 2023). However, this destabilizes the surrounding film and leads to asymmetric coatings, as shown in figure 1(*d*). A liquid coating a fibre may be stabilized by van der Waals forces (Quéré, di Meglio & Brochard-Wyart 1989) or nonlinear saturation due to flow (Quéré 1990) when the coating is thin. Thicker films may remain smooth if the coating liquid is rheologically complex, such as micelle solutions (Boulogne *et al.* 2013) and quick-curing polymer solutions (Evertz *et al.* 2021) but a general suppression mechanism for producing smooth falling threads remains elusive.

Several studies have shown that, if the axisymmetric geometry driving capillary instability is compromised using external confinement, a stable thread can persist. As first observed by Migler (2001), when a polymer blend is confined between two plates, capillary instability can be suppressed if the size of the thread is similar to the plate

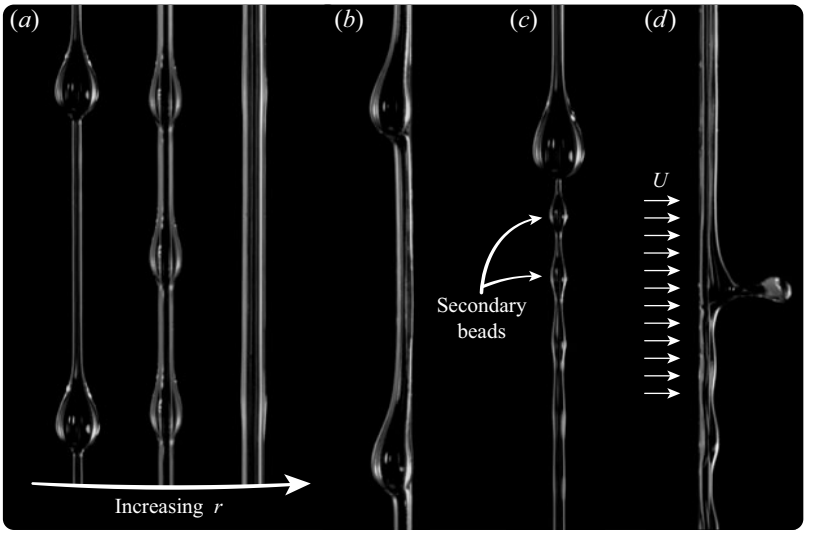

Figure 1. Bead-on-fibre instabilities. (*a*) Symmetric beading pattern with silicone oil that diminishes as the fibre radius r increases from left ($r = 0.05$ mm) to right ($r = 0.45$ mm). (*b*) Asymmetric beading patterns form for larger surface tension values, as shown for glycerol ($r = 0.25$ mm). (*c*) Secondary instabilities can develop in the thin film connecting beads, known as the isolated regime ($r = 0.05$ mm). (*d*) An applied cross-flow can change the pattern from symmetric to asymmetric, eventually causing bead detachment ($r = 0.25$ mm).

separation. A systematic study by Son *et al.* (2003) found that the confinement in a single direction requires a liquid thread to destabilize in a non-axisymmetric manner, resulting in sections of non-circular cross-section that resist capillary instability, either decreasing the growth rate while increasing the wavelength or completely suppressing the instability when confinement is strong. Additional studies have provided more detailed insight using numerical methods (Newhouse & Pozrikidis 1992; Janssen, Meijer & Anderson 2012). Shear has also been shown to suppress capillary instability (Russo & Steen 1989; Frischknecht 1998). Recently, Wang *et al.* (2020) introduced a coating technique inspired by mulberry silk that uses a dual-fibre structure to generate dip-coated films resistant to capillary instability. Their technique positions two parallel fibres in contact, altering the shape of the liquid film during dip coating into a non-circular cross-section, which effectively stabilizes it. The modified shape of the interface was estimated using the theory derived by Princen (1970) for finite volumes of liquids held statically between fibres. In this study, we expand these works to falling liquid threads and show that modifying a circular falling jet into a non-circular profile suppresses capillary instability. We adopt a similar dual-fibre system as Wang *et al.* (2020) but generalize the geometry by allowing the fibre spacing to vary and adding a base flow which extends our results to applications where closely spaced fibres are useful, such as fog harvesting (Moncuquet *et al.* 2022).

This paper begins with an overview of our experimental set-up, testing protocol and data acquisition techniques in § 2. In § 3, we examine how fibres embedded in a falling thread can deform it and provide a simple argument for thread stability based on pressure considerations. In § 4, we present our results. First, we examine the thread morphology as Q increases. Next, we map the stability threshold as it depends upon our experimental variables and present an empirical stability criterion. We then quantify the bead dynamics when the thread is unstable and derive a simple predictive scaling for the bead velocity v. Finally, we demonstrate the application of this technique to a thin geometry, specifically a

ribbon, and compare the coating stability threshold of the ribbon with that of the dual-fibre geometry. We discuss our results in § 5. In § 6, we conclude by offering some remarks on relevant applications and highlighting promising directions for future research.

2. Experiment

We performed experiments using the set-up shown in figure 2(*a*), which consists of a custom nozzle and tensioning system. Two nylon monofilament fibres (Beadalon SuppleMax) of radius r were secured inside the nozzle housing and a micrometre head was used to manually adjust their separation distance w (cf. figure 2(*a*) (inset), figure 2*b*). Here, $w = 0$ corresponds to the fibres touching. A fibre tensioning system was located at the bottom of the set-up and featured a micrometre head to ensure the fibres relative position matched that at the top of the apparatus. The fibres were tensioned to ensure the fibres did not deform due to elastocapillary adhesion (Duprat & Protiere 2015). Liquid was pumped onto the fibres through a circular nozzle of radius $r_n = 1.7$ mm at a constant flow rate Q using a NE-1000 syringe pump. The thread was recorded at a distance of 0.5 m below the nozzle using a Chronos 2.1-HD high-speed camera at 500 fps and spatial resolution around 10^{-2} mm per pixel. A mirror was placed at a 45-degree angle from the image plane to simultaneously capture the front and side views of the liquid thread. Here, the 'front view' describes the viewing plane passing through each fibre's axis while the 'side view' describes the orthogonal perspective, where the viewing plane cuts between the fibres and only a single fibre is observed, as shown in figure 2(*b*). Hereafter, we will distinguish the front and side views using superscript 'f' and 's', respectively. The experimental apparatus and optics were mounted on a pneumatically levelled optical table to minimize external vibrations and preserve spatial calibrations.

Silicone oils (Esco Products, Inc.) were used as the working liquids because they fully wet the nylon fibres, allowing the liquid thread to be significantly deformed. The density $\rho = 969\,\mathrm{kg\,m^3}$ and surface tension $\sigma = 21.1 \times 10^{-3}$ N m^{-1} were measured using an Attension Sigma 702 force tensiometer with a density probe and Wilhelmy plate, respectively. The viscosity $\mu = 9.7 \times 10^{-3}$–339×10^{-3} Pa s was measured with an Anton Paar MCR 302 shear rheometer. We quantify the liquid profile by tracking the thickness d in front and side view, and determining the maximum d_{max} and minimum d_{min} thicknesses, as shown in figure 2(*b*). Four fibres were tested with radii $r = 0.15, 0.25, 0.35$ and 0.45 mm and spacings $w = 0$–1.2 mm over a range of flow rates $Q = 2$–4000 ml hr^{-1}.

Each experiment began by attaching, levelling and tensioning two nylon fibres onto the apparatus, bringing them into contact, and then separating them by a distance w. A 10 mm calibration disk with a 0.025 mm surface tolerance was placed around the fibres and recorded as a calibration for image processing. Next, the fibres were cleaned with isopropyl alcohol and air dried. A fixed flow rate Q was then applied until the liquid thread reached steady state, after which a video was recorded for 10–30 seconds to capture the thread dynamics. Note that all steady-state profiles explored herein fully wrap the parallel fibres, in contrast to those previously observed for thin sheets bridging two parallel fibres (Gabbard & Bostwick 2023*b*).

Typical side view images of stable and unstable threads are shown in figure 2(*c*). A custom image processing code was used to quantify the thread profile. Figure 2(*d*) plots the scaled thread diameter $\bar{d} = d/r$ against time $\bar{t} = t/t_f$ for the two examples shown in figure 2(*c*), where t_f is the final time of the video. The data were fit using a Gaussian process regression model (solid black curve). Here, the maximum thickness d_{max} and

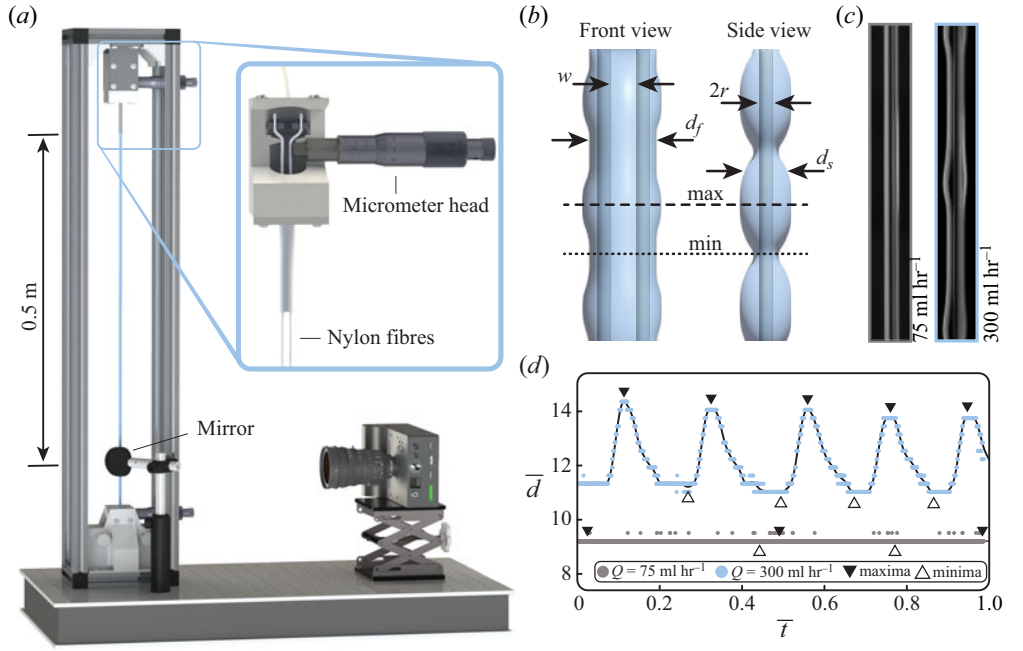

Figure 2. (*a*) Experimental set-up with inset showing the internal design of the nozzle housing. (*b*) The falling thread shown in side and front views with thicknesses d_s and d_f, respectively. (*c*) Typical experiment showing a flat fluid thread (left) for a flow rate $Q = 75$ ml hr^{-1} and wavy thread (right) for $Q = 300$ ml hr^{-1}. Here, the fluid viscosity is $\mu = 350$ m Pa s, fibre radius $r = 0.3$ mm and fibre gap $w = 0.4$ mm. (*d*) Dimensionless thread thickness $\overline{d} = d/r$ against dimensionless time $\overline{t} = t/t_f$, where t_f is the duration of the recording, for the two experiments shown in (*c*). The best-fit curve for each experiment is shown in black and the locations of the maximum d_{max} and minimum d_{min} thicknesses are denoted by the solid and hollow triangles, respectively.

minimum thickness d_{min} are identified by solid and open triangles, respectively. The same image processing code was used to quantify the thread thickness in the front view.

3. Deforming a falling liquid thread

To create a base flow with a non-circular cross-sectional shape, we deform the liquid thread internally using nylon fibres. A similar method has been used for dip coating (Wang *et al.* 2020) but here the addition of a base flow requires the fibres to pass through the nozzle to create a continuous falling thread instead of flowing bridges, which are observed if the flow is applied orthogonal to the fibre pair (Gabbard & Bostwick 2024). The liquid exits the nozzle with an axisymmetric cross-section $d^f = d^s = d_n$ but thins as it descends, as shown in figure 3(*a*).

Figure 3(*b*) plots the normalized thread diameter d/d_n, against distance from the nozzle z/l_c, as it depends upon flow rate Q for the front (dashed line) and side (solid line) views, where $l_c = \sqrt{\sigma/\rho g}$ is the capillary length with g the gravitation acceleration. For each Q, the thread reaches a uniform thickness a short distance below the nozzle. When $Q < 300$ ml hr^{-1}, the steady-state thickness is much smaller for the side view than the front view, i.e. the cross-section is non-circular. For $Q > 300$ ml hr^{-1}, the side view thickness matches the front view thickness creating a circular cross-section that increases with Q, ensuring an axisymmetric thread for all sufficiently large Q. The steady-state thickness is taken at $z/l_c = 8$ and the approximate cross-sectional shapes are

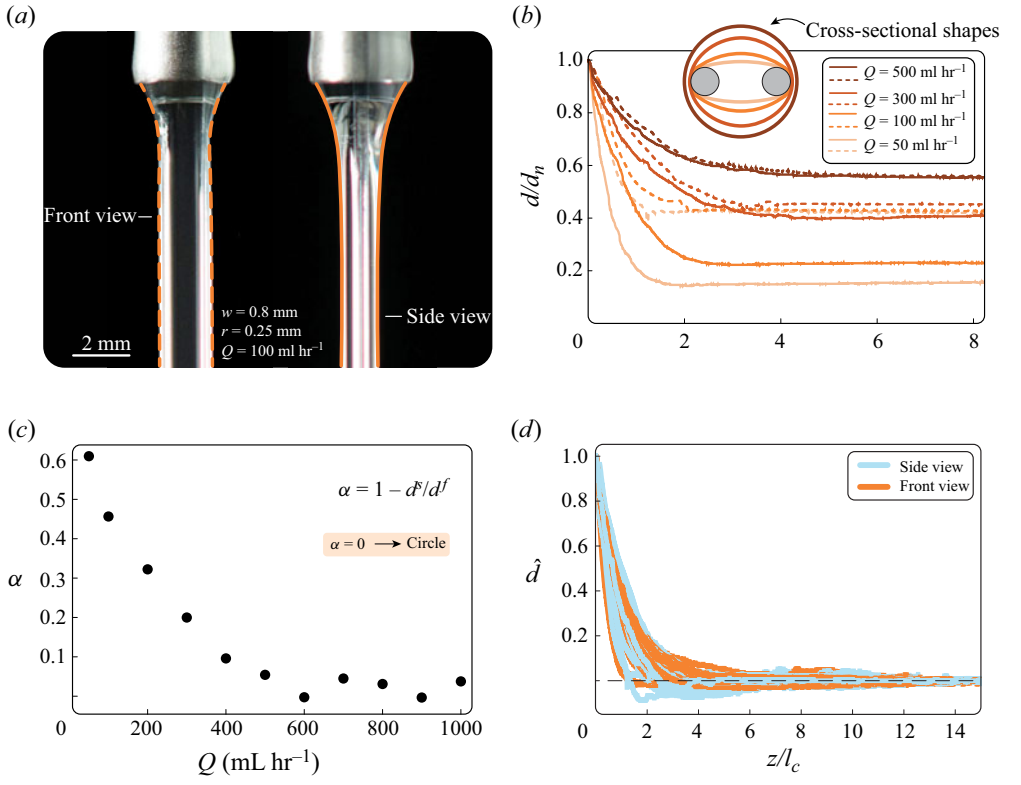

Figure 3. (*a*) Front view (left) and side view (right) of liquid deposited on two parallel fibres with radius $r = 0.25$ mm and spacing $w = 0.8$ mm at a flow rate $Q = 100$ ml hr^{-1}. The dashed and solid lines denote the liquid–air interface of the front and side view, respectively. (*b*) Normalized thread diameter d/d_n against distance from the nozzle z/l_c, where d_n is the nozzle diameter and l_c is the capillary length, as it depends on flow rate Q. Front view and side view measurements are distinguished using a dashed and solid line, respectively, with approximate cross-sectional shapes. (*c*) Thread eccentricity $\alpha = 1 - d^s/d^f$ against flow rate Q. (*d*) Normalized relative thread diameter $\hat{d} = (d_{ss} - d)/(d_{ss} - d_n)$, with d_{ss} the pre-instability steady-state thread diameter, against distance from the nozzle z/l_c for the side and front views.

overlaid on the plot with the same colour as the associated data sets. To quantify the non-circular geometry of the base flow we define the eccentricity $\alpha = 1 - d^s/d^f$, where $\alpha = 0$ corresponds to a circle and $\alpha = 1$ to a line. Figure 3(*c*) plots α against flow rate Q showing that α decreases as Q increases but steadily declines with increasing Q until a critical flow rate Q_c is reached, beyond which the thread is circular and α remains below $\alpha = 0.1$. These trends are observed for all experiments.

In our experiments we assume that any inertial–capillary 'chain oscillations' (Jordan *et al.* 2022) associated with the quick circular to non-circular shape change when $Q < Q_c$ are quickly attenuated. Figure 3(*d*) plots the normalized relative thread diameter $\hat{d} = (d_{ss} - d)/(d_{ss} - d_n)$, with d_{ss} the pre-instability steady-state thread diameter, against dimensionless distance z/l_c for all of our data in side (blue) and front (orange) views. We have defined $\hat{d}$ such that any oscillations about d_{ss} appear as oscillations about $\hat{d} = 0$. Note that several profiles exhibit 'overshoot' $\hat{d} < 0$, particularly those in the side view. This is reasonable since the initial circular thread of diameter $d = d_n$ must travel further to reach d_{ss} in the side view, especially when Q is low and w is high. In all cases, we confirm

that the inertial–capillary oscillations attenuate quickly due to viscosity, well before thread destabilization is observed $z/l_c \geq 50$ and data are recorded $z/l_c \approx 330$.

3.1. *Instability mechanism*

The presence of a wavy thread is associated with capillary instability and we seek to describe the associated instability mechanism. We begin by neglecting viscous and inertial effects and write the difference in pressure between the inside P_i and outside P_o of the thread using the Young–Laplace equation

$$\Delta P \equiv P_i - P_o = \sigma \left(\frac{1}{R_1} + \frac{1}{R_2} \right), \tag{3.1}$$

where R_1 and R_2 are the principal radii of curvature. For long wavelengths, the azimuthal curvature $1/R$ dominates axial curvature such that $\Delta P \approx \sigma/R$. The curvature of the threads we test are all concave outward, thus $\Delta P > 0$ based on our sign convention.

Figure 4 illustrates a static thread subjected to a small perturbation $\pm\epsilon$ for (*a*) $Q < Q_c$ and (*b*) $Q > Q_c$. When $Q < Q_c$, the thread is non-circular and the thickness parallel to the fibre plane is invariant to volume fluctuations, as shown earlier in figure 3(*b*). Here, the edge of the fibre maintains a thin film due to intermolecular forces, as previously observed (Wang *et al.* 2020). Thus, the perturbation acts perpendicular to the fibre plane, as shown in figure 4(*a*), where the orange curve denotes the radius of curvature for the crest (upper) R_c and trough (lower) R_t of the perturbation. Since $R_t > R_c$, the pressure is higher in the crest and a capillary flow replenishes the thin region, thereby stabilizing the thread. Alternatively, when $Q > Q_c$ the thread is circular and the response of the cross-sectional area to ϵ is shown in figure 4(*b*). Similar to the canonical Plateau–Rayleigh instability, the small perturbation results in $R_c > R_t$ and thus a capillary flow is driven from the high-pressure trough to the low-pressure crest, resulting in a wavy pattern. Unlike the Plateau–Rayleigh instability, where the capillary pressure causes breakup into drops, the presence of the fibres results in a non-circular profile stabilizing against breakup. This implies that any quasistatic thread is stable when $d^s < 2r_t$, where $r_t = 2r + w/2$. Thus, r_t is a key length scale which we will use to explore the stability of flowing threads.

3.2. *Defining the parameter space*

Having determined the stability threshold for a quasistatic thread, we now define the relevant parameters for our system with r_t being the natural length scale and $v_t = Q/r_t^2$ the characteristic velocity, which ranged from 10^{-3} to 10^0 m s^{-1}. For a general base flow governed by inertia, gravity and viscosity, one can define the Froude number $Fr \equiv v_t/(gr_t)^{1/2} \sim 10^{-5} - 10^{-2}$, which indicates the base flow in our experiments is gravity driven. A visco-gravitational number

$$\beta \equiv \rho g r_t^2/\mu v_t, \tag{3.2}$$

can be defined to characterize the base flow and ranges from 10^{-2} to 10^1. Lastly, we define the Bond number $Bo \equiv \rho g r_t^2/\sigma \sim 10^{-1} - 10^0$, indicating that both hydrostatic and capillary pressures are important, a typical feature for gravity-driven capillary phenomena like bead-on-fibre flow. Having set the characteristic length and velocity, we recast our results in dimensionless terms by using r_t and v_t as the characteristic length and velocity scales, respectively.

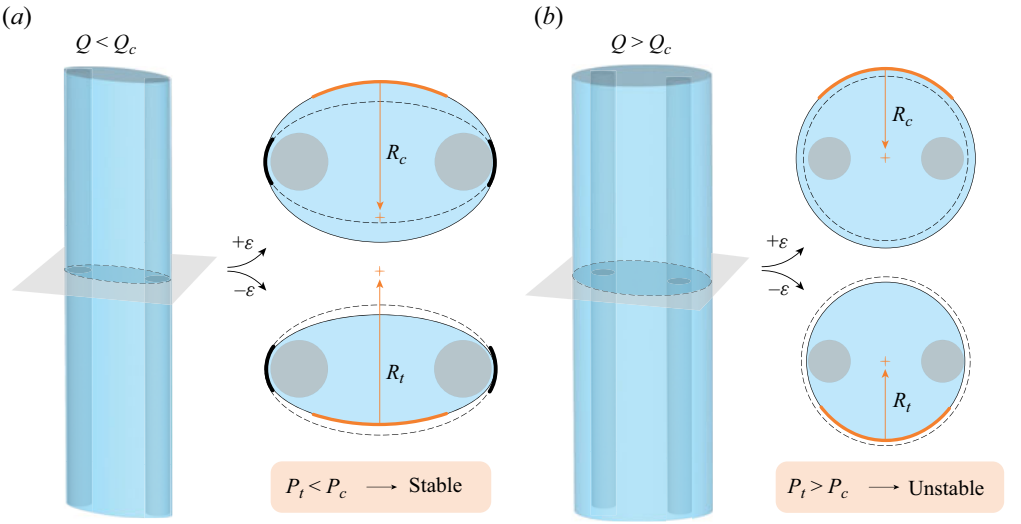

Figure 4. Illustration of instability mechanism showing a (*a*) non-circular cross-section $Q < Q_c$ and (*b*) circular cross-section for $Q > Q_c$ with associated perturbed interfaces. For $Q < Q_c$ the long edge is fixed by the edges of the fibres, such that perturbations only affect the radius of curvature R along the short edge giving rise to a stabilizing capillary flow from the crest to the trough. For $Q > Q_c$ the circular thread is always unstable due to an increased pressure (decreased curvature) at the trough, thus driving the instability.

4. Results

We have demonstrated an effective method for distorting falling liquid threads and speculated on the stability using a simple argument based on Laplace pressure. However, we have not said anything about the temporal evolution of the thread and its spatial structure. In this section, we quantify the thread morphology, stability threshold and bead dynamics.

4.1. *Thread morphology*

Figure 5(*a*) shows side view images of a falling thread for increasing flow rate Q from $Q = 2$ to $Q = 150$ ml hr^{-1}. Here, we observe a clear transition from a uniform (stable) thread to a wavy (unstable) thread with the dynamics shown in the Supplemental Material, Movie 1 available at https://doi.org/10.1017/jfm.2024.1091. Figure 5(*b–d*) quantifies the shape of the thread by plotting (*b*) the average maximum thread diameter d_{max}, (*c*) the average minimum thread diameter d_{min} and (*d*) the dimensionless amplitude of the undulations $\tilde{a} = a/r_t$, where $a = d_{max} - d_{min}$, against Q. For low Q, d_{max} and d_{min} increase linearly with Q in the side view, but remain constant in the front view. This represents a non-circular cross-section which becomes more circular as Q increases. Above a critical flow rate Q_c, d_{max} and d_{min} increase at similar rates irrespective of perspective and have similar d_{max}, indicating a circular cross-section. Interestingly, d_{min} is always larger in the front view. This mismatch corresponds to a non-circular region connecting the circular beads, which is opposite to that observed with capillary instability in external confinement (Son *et al.* 2003). For both a free-falling jet and flow down a fibre this region has a circular cross-section, leading to drop pinchoff and a secondary bead-on-fibre pattern, respectively. This between-beads stability agrees with our simple stability argument described in § 3.1, such that when $Q > Q_c$ a cylindrical base state will (i) thicken in regions that terminate as a bead with circular cross-section, as observed, and (ii) thin between beads until the

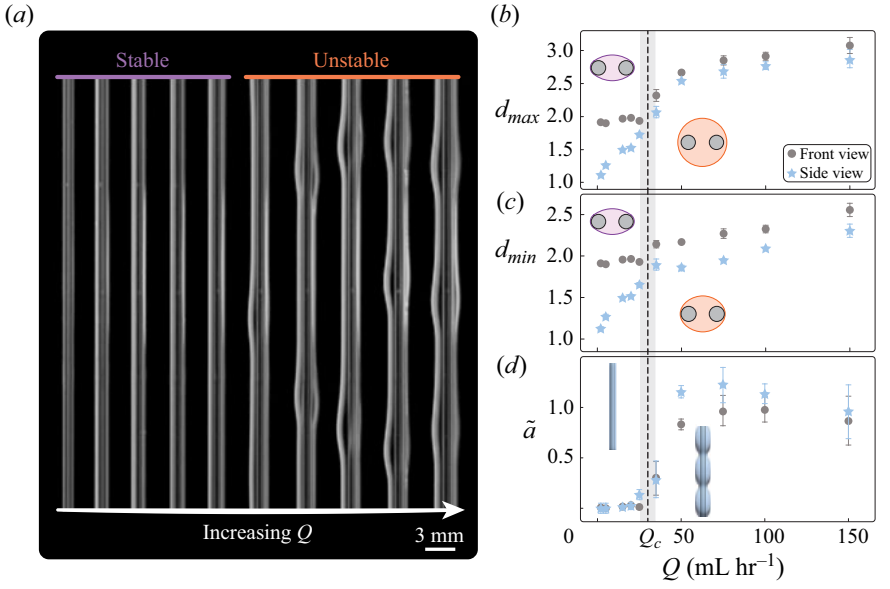

Figure 5. (*a*) Thread destabilization as the flow rate Q increases from left to right showing stable and unstable threads. Here, $r = 0.25$, $w = 0.2$ mm and $\mu = 339$ m Pa s. Scale bar is 3 mm long. (*b*) Maximum thread diameter d_{max}, (*c*) minimum thread diameter d_{min} and (*d*) dimensionless amplitude $\tilde{a} = a/r_t$ against Q as measured in front (grey circle) and side view (blue star). The vertical black line denotes the stability threshold $Q = Q_c$. Inset illustrations show the approximate cross-sectional shape for $Q < Q_c$ (purple) and $Q > Q_c$ (orange).

thread regains stability at $d_{min} \approx 2r_t$. However, what is not predicted is that the thread thins beyond the minimum circular profile that result in non-circular neck regions. Lastly, we note that, below Q_c, the amplitude of interfacial undulations $\tilde{a}$ is negligible but sharply increases as Q_c is surpassed, as shown in figure 5(*d*). Just above Q_c, $\tilde{a}$ is greater in the side view than the front view since the fibres prevent large fluctuations parallel with the fibre plane. As Q further increases, the average thread thickness increases, allowing larger fluctuations perpendicular to the fibre plane until $\tilde{a}$ is independent of perspective.

4.2. *Stability threshold*

Next, we explore how the critical flow rate Q_c depends on the characteristic length r_t and viscosity μ. Figure 6(*a*) plots Q_c against r_t, as it depends upon fibre radius r. As r_t increases, Q_c increases since more volume is required to form a circular thread large enough to encompass both fibres. The data collapse along a single trend, confirming that r_t, not the fibre radius r or spacing w, is the appropriate length scale. Furthermore, the data follow a $Q_c \sim r_t^4$ scaling, as shown by the dashed line. Figure 6(*b*) plots Q_c against r_t, as it depends upon μ. The data no longer collapse upon a single trend as increasing μ for a given Q thickens the thread. A positive trend between Q_c and r_t is observed for all μ while for a fixed r_t, increasing μ leads to a decrease in Q_c. This was also observed for parallel fibres being dip coated, where the capillary number Ca controls the coating thickness and thus increasing μ (equivalently, Ca) leads to capillary instability at lower withdrawal velocity (Wang *et al.* 2020).

The stability of a quasi-static thread depends solely on the cross-sectional geometry. Here, we assume the system geometry also defines the stability boundary through the

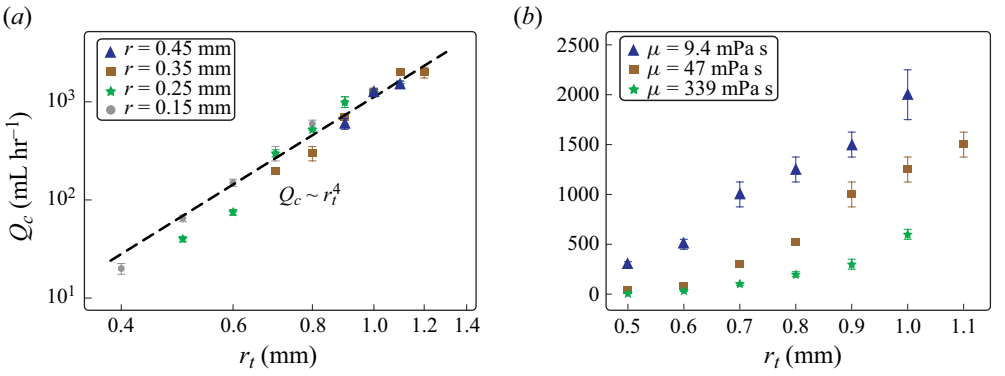

Figure 6. (*a*) Critical flow rate Q_c against the characteristic length r_t, as it depends upon fibre radius r for viscosity $\mu = 47$ m Pa s. The data fall along the curve $Q_c \sim r_t^4$. (*b*) Value of Q_c against r_t as it depends upon μ for $r = 0.25$ mm.

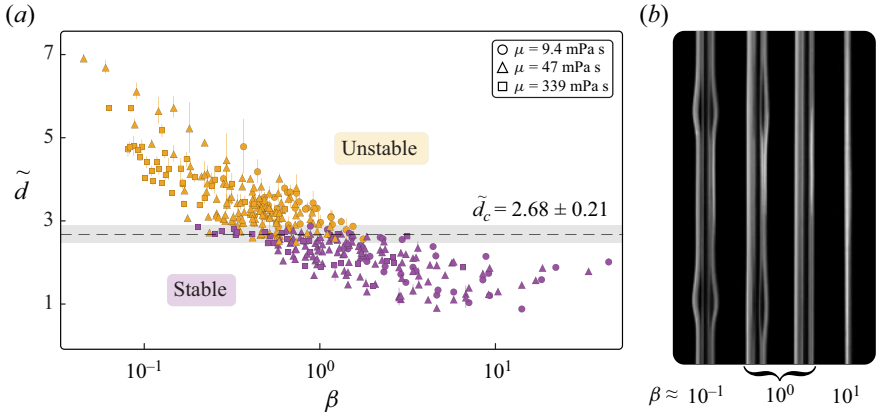

Figure 7. (*a*) Stability diagram showing stable (purple) and unstable (orange) threads by plotting dimensionless maximum diameter $\tilde{d} = d^s_{max}/r_t$ against visco-gravitational number $\beta = \rho g r_t^4/\mu Q$. The dashed line denotes the stability threshold $\tilde{d}_c = 2.68 \pm 0.21$ with the shaded region showing the empirical overlap. Plot markers indicate the viscosity of each test. (*b*) Side view images for different β with $\tilde{d} = 4.8$, 2.5, 2.1 and 2, from left to right.

side view diameter d^s. Figure 7(*a*) plots the dimensionless maximum thread diameter $\tilde{d} = d^s_{max}/r_t$ against visco-gravitational number β, with coloured markers differentiating stable (purple) and unstable (orange) threads for all of our experimental data. A stability threshold emerges, primarily as a function of $\tilde{d}$ but noticeably larger than that for quasi-static coatings $\tilde{d}_c = 2$. Here, the threshold $\tilde{d} = 2.68 \pm 0.21$ is shown by the dashed line and the overlap region in the data is shaded grey. Thus, thread stability is due to the growth of the thread beyond a critical thickness, which is larger than that predicted for a quasi-static coating. This finding is consistent with the measured film thickness along the edges of the fibres from the front view, which is assumed negligibly thin for quasi-static coatings, but is of the order 0.1 mm in our experiments. Figure 7(*b*) shows threads for $\beta \approx 10^{-1}$ (left), $\beta \approx 10^0$ (middle) and $\beta \approx 10^1$ (right). Apparent in the data and demonstrated by these images is the transition in stability as β changes and the transition region $\beta \approx 1$ where threads may exhibit a flat or wavy thread.

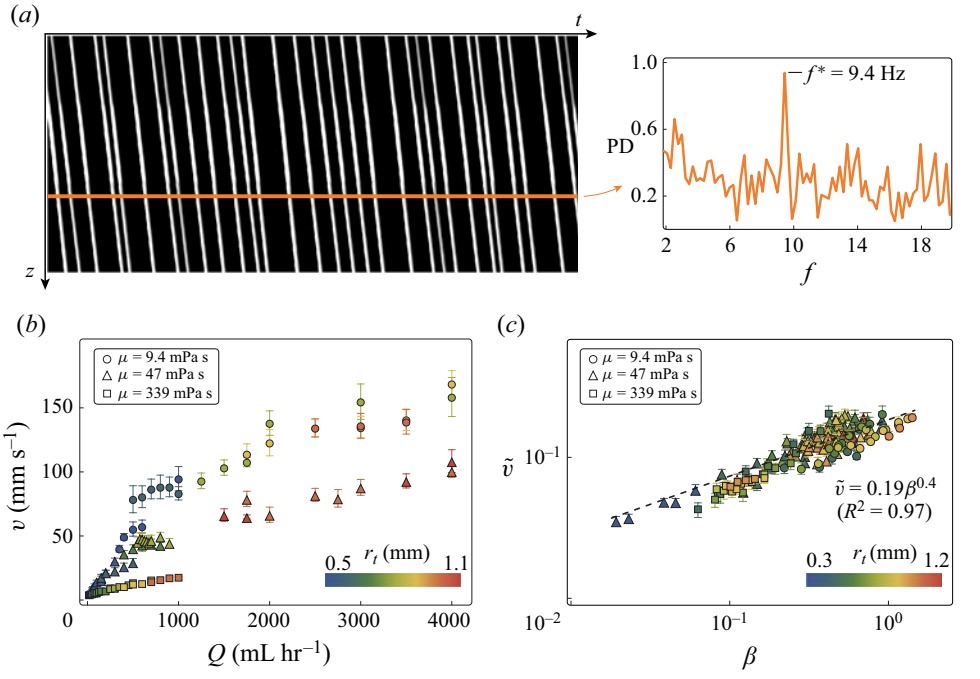

Figure 8. (*a*) Typical spatio-temporal diagram with beads shown in white for $r = 0.25$ mm and $w = 1$ mm. The thread profile is tracked at a fixed vertical location (horizontal orange line) and the power density (PD) is determined using an FFT. (*b*) Bead velocity v against flow rate Q, as it depends upon viscosity μ. (*c*) Dimensionless bead velocity $\tilde{v} = v/v_t$, where $v_t = Q/r_t^2$, against visco-gravitational number $\beta = \rho g r_t^4/\mu Q$ exhibits a power-law trend with exponent $n = 2/5$ and coefficient of determination $R^2 = 0.96$. The colour bars in (*b*,*c*) indicate the characteristic length r_t.

4.3. *Bead dynamics*

Once the thread diameter surpasses the stability threshold $\tilde{d} = 2.68 \pm 0.21$, the film destabilizes into a series of beads flowing down a stable film, which ensures no dry spots develop. The bead dynamics exhibits a temporal and spatial dependence. Figure 8(*a*) shows a spatio-temporal diagram constructed by tracking a column of pixels intersecting the widest sections (beads) of the film, thereby showing the spatio-temporal evolution of the flow. The reader may find the movie corresponding to this spatio-temporal diagram in the Supplemental Material, Movie 2. The white lines indicate bead locations and their slope gives the bead velocity. The lines are not parallel because interactions between the beads have rearranged their structure. If we track the thread diameter at a fixed vertical position we can construct the thread profile. Then, applying a fast Fourier transform (FFT) reveals the frequency spectrum, which shows a maximum frequency $f^* = 9.4$ Hz that varies slightly with time and location along the fibre. Interactions between the beads result in a signal with finite bandwidth, an observation previously made for convectively unstable flow down a fibre (Duprat *et al.* 2007). This behaviour is expected for high Q, where the flow advection time decreases relative to the linear growth time of the capillary instability. In our experiments, this is typical, as beads only emerge for high flow rates $Q \geq Q_c$ and result in global behaviour similar to that shown in figure 8(*a*).

Due to convective interactions, the bead velocity v varies but remains bounded within an associated error for each experiment. Figure 8(*b*) plots v against flow rate Q for three

different viscosities μ and $r = 0.25$ mm. The marker colours reflect the characteristic length r_t for each experiment. For all μ, v increases with Q. As expected, decreasing μ increases v. Despite the base flow being convectively unstable, v follows a clear trend and motivates us to explore a simple scaling argument to describe the bead dynamics.

Neglecting capillary effects, we can balance the gravitational energy rate

$$\Phi_g \approx \rho g V v, \tag{4.1}$$

with the viscous dissipation

$$\Phi_\mu \approx 2\zeta\mu \left(\frac{\partial v}{\partial r}\right)^2 V, \tag{4.2}$$

where ζ is a dissipation coefficient. The energy rate balance is then

$$\rho g V v = \zeta \frac{2\mu V v^2}{r_t^2}, \tag{4.3}$$

which we can rearrange and non-dimensionalize to find

$$\frac{v}{v_t} \sim \frac{1}{\zeta}\frac{\rho g r_t^4}{2\mu}. \tag{4.4}$$

Here, the left-hand side is our dimensionless velocity $\tilde{v} = v/v_t = v r_t^2/Q$ and the right-hand side contains the visco-gravitational number β.

Figure 8(c) plots $\tilde{v}$ against β for all our experiments. The shape and colour of the data markers indicate μ and r_t, respectively. The data follow a power-law trend $\tilde{v} \sim \beta^{0.4}$ with coefficient of determination $R^2 = 0.97$, indicating a significant trend between v and the visco-gravitational number β. This scaling law is a robust predictor of v when the flow is visco-gravitational but may become invalid at higher Q, when the flow is visco-inertial. This transition has been explored for flow down a fibre (Ruyer-Quil & Kalliadasis 2012) but remains unexplored for liquid coating multiple fibres.

4.4. *The slender geometry limit $\Lambda << 1$: coating a ribbon*

This method for suppressing capillary instability can be extended to other slender geometries. For example, we coated a vertically oriented nylon ribbon with a rectangular cross-section of thickness $a \approx 0.01$ mm and width $b \approx 3$ mm. This geometry presented two distinct changes from the dual-fibre system. First, the aspect ratio associated with its cross-section $\Lambda = a/b \approx 0.03$ is much lower than any tested for the dual-fibre system $\Lambda = r/r_t \geq 0.17$, a feature which renders the ribbon thickness negligible and creates a singularity in the capillary pressure, as we will see. Second, the ribbon can block liquid from passing from one side to the other, unlike the dual-fibre system where liquid may pass between the fibres. Figure 9(b) shows the coated ribbon with flow rate Q increasing from left to right. For low Q, the ribbon is coated with a stable thin film of uniform thickness. Similar to the dual-fibre system, increasing Q beyond a critical value results in capillary instability, as shown by the images under the orange bar. Thus, suppression of capillary instability for coatings on non-axisymmetric geometries is a general feature that can be expected for most wettable slender structures.

We quantify the ribbon coatings shown in figure 9(b) using the thread thickness as measured from the side view d^s. Figure 9(c) plots d^s against Q with maximum and minimum thickness denoted by grey circles and blue stars, respectively. The result

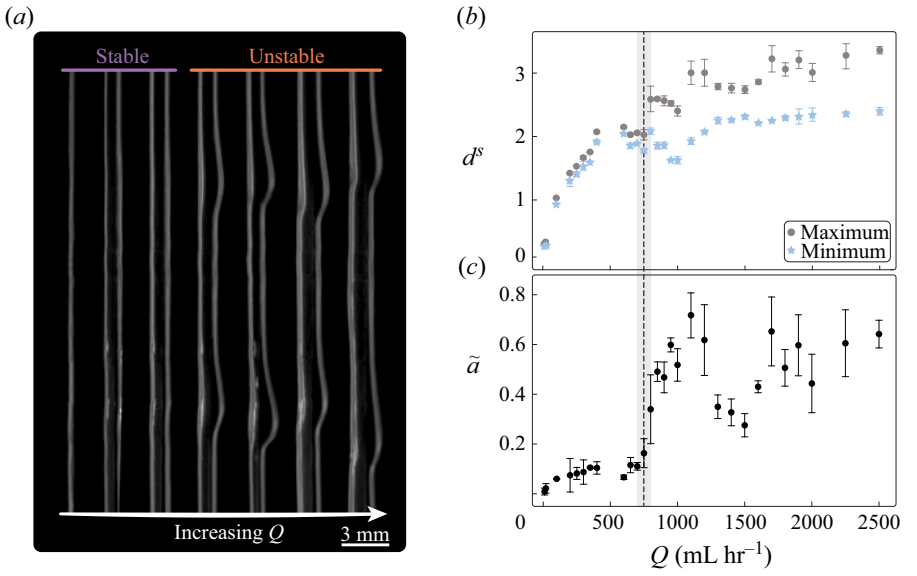

Figure 9. (*a*) Silicone oil ($\mu = 47$ m Pa s) flowing down a nylon ribbon of thickness $a = 0.01$ mm and width $b = 3$ mm exhibits instability as the flow rate increases from left to right. Scale bar is 3 mm long. (*b*) Maximum (grey circles) and minimum (blue star) thread diameter d^s measured perpendicular to the ribbon width and (*c*) dimensionless wave amplitude $\tilde{a} = a/r_t$, with $r_t = b/2 = 1.5$ mm, against flow rate Q. For low Q, the maximum and minimum thread diameters are similar and $\tilde{a}$ is small. For high Q, the film is unstable causing the maximum and minimum thread diameter to diverge and $\tilde{a}$ to increase.

mirrors those shown in figure 5, where below a critical flow rate Q_c the thread has little thickness variations, but above Q_c beads emerge, as indicated by the large difference in the maximum and minimum thicknesses. Figure 5(*d*) plots the bead amplitude $a = a/r_t$, where $a = d^s_{max} - d^s_{min}$ and $r_t = b/2 = 1.5$ mm, against Q and shows that above a critical flow rate $Q_c \approx 750$ *ml*/hr, a increases from below 0.1 to as high as 0.7. These results are qualitatively similar to those for parallel fibres, but a quantitative inspection reveals a distinct difference. In figure 9(*c*) the thread begins to lose stability when $d^s \approx 2$ mm, which is less than the width of the ribbon $b = 3$ mm. Thus, the dimensionless maximum diameter is $\widetilde{d}_c \approx 1.3$, much lower than $\widetilde{d}_c \approx 2.68$ for parallel fibres. Additionally, this value seems to contradict the instability analysis, which indicated a stable thread for $\tilde{d} < 2$. This result may be explained by the two distinctions between the ribbon geometry and parallel fibres mentioned in the previous paragraph. Since the capillary pressure is proportional to the interfacial curvature, the pressure diverges for negligibly small thicknesses – like those common in ribbons – and a singularity in the capillary pressure is approached, resulting in spontaneous dewetting at the ribbon edge despite the coatings smooth initial profile. This has been observed for oval fibres (Alimov & Kornev 2014) with Zhang & Kornev (2017) demonstrating rapid dewetting and contact line formation around the edges of dip-coated ribbons, where the resulting pinned contact line effectively isolates the fluid on each side of the ribbon. These features explain the reduced transition threshold and the asymmetric beads observed in figure 9(*b*). Thus, capillary suppression is observed for many slender structures beyond the parallel-fibre system but additional physics associated with contact line formation and dewetting can lower the stability threshold and result in asymmetric bead patterns. These features remain an open area for exploration.

5. Discussion

This study explored an effective means for suppressing capillary instability that differed from previous studies by using internal distortion instead of external confinement. When a thread is unconstrained, perturbations grow despite the increased interfacial free energy associated with additional axial contour length because the average radius of the thread must decrease to conserve volume. Hence, sinusoidal perturbations in a two-dimensional section always decay (San Miguel, Grant & Gunton 1985). In three dimensions, an asymmetric external confinement causes perturbations to grow asymmetrically, and the increase in free energy from contour lengthening outweighs the energy decrease from a decreasing thread size, thereby suppressing the instability or altering its wavelength and shape (Son *et al.* 2003). If the confinement is imposed with azimuthal symmetry, such as a cylindrical thread in a similar-sized tube, the thread remains unstable but with altered dynamics (Hagedorn, Martys & Douglas 2004). The internal distortion method presented here forces the initial profile to be non-circular which ensures perturbations decay below the stability threshold. Once $Q > Q_c$, the initial profile is circular, akin to the starting profile for external confinement but the final profile is different. For example, for moderate external confinement, where perturbations grow to form an undulated thread, the neck regions are far from the confinement and thus have a circular cross-section where the bulging regions approach the bounding plates and become elongated in the orthogonal direction. For internal confinement using parallel fibres, the opposite is observed, the beads take on a circular shape since they do not feel the fibres but the neck region has an oval shape which results from the hydrodynamic interactions between the film and fibres and stabilizes it.

The physical reasoning underlying our results is mostly based on geometric considerations but some of the finer physical details require further study, such as the thickness of the film coating the outermost edges of the fibres, which is approximately 10^{-1} mm but plays a seemingly negligible role in defining the stability threshold. Furthermore, the stability of the film in this region is compromised when the object to be coated is too slender, as demonstrated in figure 9 for a ribbon. How the aspect ratio $\Lambda = a/b$ alters the stability threshold and bead dynamics remains an open topic. Additionally, the shape of beads formed when a well-wetting liquid flows down a dual-fibre system requires further analysis. Specifically, we notice that beads often emerge with slight asymmetry, as shown in figure 5. We have found that a base flow delays the onset of Plateau–Rayleigh instability to larger film thicknesses compared with a static coating (Wang *et al.* 2020), which reflects previous findings for thin coatings on vertical fibres where flow can prevent bead growth (Quéré 1990) and requires further inspection. Lastly, the extension from parallel fibres to a ribbon was an illustrative example of a system with low aspect ratio and an impermeable interior but a more natural extension would be arrays of more than two fibres arranged in a radial pattern. Multi-fibre arrays were considered in prior theoretical studies (Princen 1970) and could provide finer control of capillary instability, especially for large threads. We expect a similar geometric stability criteria as that explored here to govern the flow evolution.

6. Conclusion

In this study we demonstrated a method for suppressing capillary instability whereby two vertical fibres encased in a liquid thread internally distort the thread's cross-sectional shape. Image analysis revealed a shape transition from a circular to a non-circular profile when the flow rate Q was below a critical value Q_c. The thread morphology

was evaluated down the fibre and a transition in the base state from non-circular to circular shape correlated with the appearance of beads flowing down the fibres. The role of the experimental variables on thread stability was explored over a large range of values. The stability threshold was found to be mostly geometrical, where stable threads are readily observed when $\tilde{d} < \widetilde{d}_c = 2.68 \pm 0.21$. When $\tilde{d} > \widetilde{d}_c$, capillary flow inside the thread forms flowing beads, akin to the bead-on-fibre patterns observed in flow down a fibre. Since high Q are required to produce unstable threads ($\tilde{d} > \widetilde{d}_c$), the base flow is typically convectively unstable, resulting in convective interaction between beads. Despite this, the average bead velocity v showed a power-law correlation with the visco-gravitational number $\beta = \rho g r_t^4/\mu Q$, as predicted by our simple scaling analysis. Lastly, we extended this method of capillary suppression to other slender geometries. The suppression technique is effective but the non-permeable structure and the ultra-thin ribbon thickness caused contact line formation that isolates the liquid on each side of the ribbons long edge and leads to an earlier onset of bead formation, which have an asymmetric profile.

This suppression method has application in many settings due to the ubiquity of liquid threads and their intrinsic destabilization into drops or beads. In fibre coating applications, two neighbouring fibres coated simultaneously can avoid both bead formation and dewetting and we expect a similar uniform coating could exist when coating fibre bundles below a critical flow rate. This has already been shown theoretically for capillary rise and finite volumes of liquid within multi-fibre systems by Princen (1970) and Lukáš *et al.* (2006) but has yet to be empirically shown for a system where the liquid encases the fibres. Determining the stability threshold for liquid coating multiple fibres is thus a fruitful topic for exploration since many bioinspired wetting and droplet transport techniques leverage fibre bundles (Meng *et al.* 2014; Wang *et al.* 2017) and liquid–textile interactions require considering liquid interaction with multiple fibres (Minor *et al.* 1959; Duprat 2022). These results also provide an efficient means for manufacturing parallel electrical wire encased in a curable sheath either by a continuous base flow, as shown here, or by dip coating (Wang *et al.* 2020).

In many scenarios the breakup of a column into drops or beads is undesirable, which gives a direct need for suppression of capillary instability. However, in some applications the beads are useful, as evidenced by the recent push to use bead-on-fibre flows for heat and mass transfer applications, such as desalination (Sadeghpour *et al.* 2019), particle capturing (Sadeghpour *et al.* 2021), moisture capturing (Labbé & Duprat 2019; Nguyen *et al.* 2021; Moncuquet *et al.* 2022), heat exchange (Zeng *et al.* 2017; Wagstaff *et al.* 2023) and gas absorption (Chinju, Uchiyama & Mori 2000; Uchiyama *et al.* 2003; Grünig *et al.* 2012; Hosseini *et al.* 2014). In these applications, flow down parallel fibres can safeguard against undesired 'dry spots' that occur in flow down a fibre due to secondary Plateau–Rayleigh instability (see figure 1*c*). The stability of the non-circular neck regions between beads, coupled with our simple scaling for the bead velocity, make flow down fibre pairs an effective means for applications requiring predictable thread stability and bead dynamics. Additionally, flow between fibres has been observed in water harvesting with fibre arrays (Shi *et al.* 2018; Moncuquet *et al.* 2022) and Labbé & Duprat (2019) explored the efficiency of a dual-fibre system for capturing aerosol droplets. Our results assist in advancing the current state of water harvesting using fibre arrays by providing critical insight into when a film between a fibre pair will destabilize into beads, which descend and drip from the mesh, purging the system and restoring stability.

This study marks another fundamental step in suppressing capillary instability by considering a base flow down parallel fibres with adjustable spacing, allowing for larger threads to be stabilized. Despite this advancement, many practical and physically intriguing questions remain, such as the role of the aspect ratio Λ on thread stability, the behaviour of non-wetting liquids and how the fibre material alters the flow morphology. Lastly, we note that, while this study focused on viscous flow, many applications use water or low-viscosity liquids with non-negligible inertial forces where Kapitza instability may be the favourable destabilization mechanism (Kapitza 1948). Although external confinement has been shown to suppress this instability mechanism (Lavalle *et al.* 2019) and low-viscosity liquid sheets between fibres can avoid breakup (Gabbard & Bostwick 2023*b*), more research is needed focused on flow down parallel fibres to provide a compressive understanding across all practical flow conditions.

Supplementary movies. Supplementary movies are available at https://doi.org/10.1017/jfm.2024.1091.

Funding. J.B.B. acknowledges support from NSF Grant CMMI-1935590. This project is partially supported by the Clemson University Creative Inquiry program.

Declaration of interests. The authors report no conflict of interest.

Author ORCIDs.
Chase T. Gabbard https://orcid.org/0009-0006-4412-4066;
Joshua B. Bostwick https://orcid.org/0000-0001-7573-2108.

References

ALIMOV, M.M. & KORNEV, K.G. 2014 Meniscus on a shaped fibre: singularities and hodograph formulation. *Proc. R. Soc.* A **470** (2168), 20140113.

BOULOGNE, F., FARDIN, M.-A., LEROUGE, S., PAUCHARD, L. & GIORGIUTTI-DAUPHINÉ, F. 2013 Suppression of the Rayleigh–Plateau instability on a vertical fibre coated with wormlike micelle solutions. *Soft Matt.* **9** (32), 7787–7796.

CAMASSA, R., OGROSKY, H.R. & OLANDER, J. 2014 Viscous film flow coating the interior of a vertical tube. Part 1. Gravity-driven flow. *J. Fluid Mech.* **745**, 682–715.

CAZAUBIEL, A. & CARLSON, A. 2023 Influence of wind on a viscous liquid film flowing down a thread. *Phys. Rev. Fluids* **8** (5), 054002.

CHANG, H.-C. & DEMEKHIN, E.A. 1999 Mechanism for drop formation on a coated vertical fibre. *J. Fluid Mech.* **380**, 233–255.

CHINJU, H., UCHIYAMA, K. & MORI, Y.H. 2000 'string-of-beads' flow of liquids on vertical wires for gas absorption. *AIChE J.* **46** (5), 937–945.

CRASTER, R.V. & MATAR, O.K. 2006 On viscous beads flowing down a vertical fibre. *J. Fluid Mech.* **553**, 85–105.

DUPRAT, C. 2022 Moisture in textiles. *Annu. Rev. Fluid Mech.* **54**, 443–467.

DUPRAT, C. & PROTIERE, S. 2015 Capillary stretching of fibers. *Europhys. Lett.* **111** (5), 56006.

DUPRAT, C., RUYER-QUIL, C., KALLIADASIS, S. & GIORGIUTTI-DAUPHINÉ, F. 2007 Absolute and convective instabilities of a viscous film flowing down a vertical fiber. *Phys. Rev. Lett.* **98** (24), 244502.

EGGERS, J. & DUPONT, T.F. 1994 Drop formation in a one-dimensional approximation of the Navier–Stokes equation. *J. Fluid Mech.* **262**, 205–221.

EGHBALI, S., KEISER, L., BOUJO, E. & GALLAIRE, F. 2022 Whirling instability of an eccentric coated fibre. *J. Fluid Mech.* **952**, A33.

EVERTZ, A., SCHREIN, D., OLSEN, E., HOFFMANN, G.-A. & OVERMEYER, L. 2021 Dip coating of thin polymer optical fibers. *Opt. Fiber Technol.* **66**, 102638.

FRENKEL, A.L. 1992 Nonlinear theory of strongly undulating thin films flowing down vertical cylinders. *Europhys. Lett.* **18** (7), 583.

FRISCHKNECHT, A. 1998 Stability of cylindrical domains in phase-separating binary fluids in shear flow. *Phys. Rev.* E **58** (3), 3495.

GABBARD, C.T. & BOSTWICK, J.B. 2021 Asymmetric instability in thin-film flow down a fiber. *Phys. Rev. Fluids* **6** (3), 034005.

GABBARD, C.T. & BOSTWICK, J.B. 2023*a* Bead-on-fibre morphology in shear-thinning flow. *J. Fluid Mech.* **961**, A14.

GABBARD, C.T. & BOSTWICK, J.B. 2023*b* Thin film flow between fibers: inertial sheets and liquid bridge patterns. *Phys. Rev. Fluids* **8** (11), 110505.

GABBARD, C.T. & BOSTWICK, J.B. 2024 Gravity-driven flow of liquid bridges between vertical fibres. *J. Fluid Mech.* **997**, A74.

GALLAIRE, F. & BRUN, P.-T. 2017 Fluid dynamic instabilities: theory and application to pattern forming in complex media. *Phil. Trans. R. Soc.* A **375** (2093), 20160155.

GRÜNIG, J., LYAGIN, E., HORN, S., SKALE, T. & KRAUME, M. 2012 Mass transfer characteristics of liquid films flowing down a vertical wire in a counter current gas flow. *Chem. Engng Sci.* **69** (1), 329–339.

HAGEDORN, J.G., MARTYS, N.S. & DOUGLAS, J.F. 2004 Breakup of a fluid thread in a confined geometry: droplet-plug transition, perturbation sensitivity, and kinetic stabilization with confinement. *Phys. Rev.* E **69** (5), 056312.

HOSSEINI, S.M., ALIZADEH, R., FATEHIFAR, E. & ALIZADEHDAKHEL, A. 2014 Simulation of gas absorption into string-of-beads liquid flow with chemical reaction. *Heat Mass Transfer* **50**, 1393–1403.

JANSSEN, P.J.A., MEIJER, H.E.H. & ANDERSON, P.D. 2012 Stability and breakup of confined threads. *Phys. Fluids* **24** (1), 012102.

JORDAN, D.T.A., RIBE, N.M., DEBLAIS, A. & BONN, D. 2022 Chain oscillations in liquid jets. *Phys. Rev. Fluids* **7** (10), 104001.

KALLIADASIS, S. & CHANG, H.-C. 1994 Drop formation during coating of vertical fibres. *J. Fluid Mech.* **261**, 135–168.

KAPITZA, P.L. 1948 Wave flow of thin viscous fluid layers. *Zh. Eksp. Teor. Fiz.* **18**, 3–28.

KLIAKHANDLER, I.L., DAVIS, S.H. & BANKOFF, S.G. 2001 Viscous beads on vertical fibre. *J. Fluid Mech.* **429**, 381–390.

LABBÉ, R. & DUPRAT, C. 2019 Capturing aerosol droplets with fibers. *Soft Matt.* **15** (35), 6946–6951.

LAVALLE, G., LI, Y., MERGUI, S., GRENIER, N. & DIETZE, G.F. 2019 Suppression of the Kapitza instability in confined falling liquid films. *J. Fluid Mech.* **860**, 608–639.

LUKÁŠ, D., CHALOUPEK, J., KOŠŤÁKOVÁ, E., PAN, N. & MARTINKOVA, I. 2006 Morphological transitions of capillary rise in a bundle of two and three solid parallel cylinders. *Physica* A **371** (2), 226–248.

MENG, Q., WANG, Q., LIU, H. & JIANG, L. 2014 A bio-inspired flexible fiber array with an open radial geometry for highly efficient liquid transfer. *NPG Asia Mater.* **6** (9), e125–e125.

MIGLER, K.B. 2001 String formation in sheared polymer blends: coalescence, breakup, and finite size effects. *Phys. Rev. Lett.* **86** (6), 1023.

MINOR, F.W., SCHWARTZ, A.M., WULKOW, E.A. & BUCKLES, L.C. 1959 The migration of liquids in textile assemblies. Part 2. The wicking of liquids in yams. *Text. Res. J.* **29** (12), 931–939.

MONCUQUET, A., MITRANESCU, A., MARCHAND, O.C., RAMANANARIVO, S. & DUPRAT, C. 2022 Collecting fog with vertical fibres: combined laboratory and in-situ study. *Atmos. Res.* **277**, 106312.

NEWHOUSE, L.A. & POZRIKIDIS, C. 1992 The capillary instability of annular layers and liquid threads. *J. Fluid Mech.* **242**, 193–209.

NGUYEN, L.T., BAI, Z., ZHU, J., GAO, C., LIU, X., WAGAYE, B.T., LI, J., ZHANG, B. & GUO, J. 2021 Three-dimensional multilayer vertical filament meshes for enhancing efficiency in fog water harvesting. *ACS Omega* **6** (5), 3910–3920.

PLATEAU, J. 1873 *Statique expérimentale et théorique des liquides soumis aux seules forces moléculaires*. Tome Second, Gauthier-Villars.

PRINCEN, H.M. 1970 Capillary phenomena in assemblies of parallel cylinders. III. Liquid columns between horizontal parallel cylinders. *J. Colloid Interface Sci.* **34** (2), 171–184.

QUÉRÉ, D. 1990 Thin films flowing on vertical fibers. *Europhys. Lett.* **13** (8), 721.

QUÉRÉ, D. 1999 Fluid coating on a fiber. *Annu. Rev. Fluid Mech.* **31** (1), 347–384.

QUÉRÉ, D., DI MEGLIO, J.-M. & BROCHARD-WYART, F. 1989 Making van der waals films on fibers. *Europhys. Lett.* **10** (4), 335.

RAYLEIGH, LORD 1878 On the instability of jets. *Proc. Lond. Math. Soc.* **1** (1), 4–13.

RUSSO, M.J. & STEEN, P.H. 1989 Shear stabilization of the capillary breakup of a cylindrical interface. *Phys. Fluids* A **1** (12), 1926–1937.

RUYER-QUIL, C. & KALLIADASIS, S. 2012 Wavy regimes of film flow down a fiber. *Phys. Rev.* E **85** (4), 046302.

RUYER-QUIL, C., TREVELEYAN, P., GIORGIUTTI-DAUPHINÉ, F., DUPRAT, C. & KALLIADASIS, S. 2008 Modelling film flows down a fibre. *J. Fluid Mech.* **603**, 431–462.

SADEGHPOUR, A., OROUMIYEH, F., ZHU, Y., KO, D.D., JI, H., BERTOZZI, A.L. & JU, Y.S. 2021 Experimental study of a string-based counterflow wet electrostatic precipitator for collection of fine and ultrafine particles. *J. Air Waste Manage.* **71** (7), 851–865.

SADEGHPOUR, A., ZENG, Z., JI, H., DEHDARI EBRAHIMI, N., BERTOZZI, A.L. & JU, Y.S. 2019 Water vapor capturing using an array of traveling liquid beads for desalination and water treatment. *Sci. Adv.* **5** (4), eaav7662.

SAN MIGUEL, M., GRANT, M. & GUNTON, J.D. 1985 Phase separation in two-dimensional binary fluids. *Phys. Rev.* A **31** (2), 1001.

SHI, W., ANDERSON, M.J., TULKOFF, J.B., KENNEDY, B.S. & BOREYKO, J.B. 2018 Fog harvesting with harps. *ACS Appl. Mater. Inter.* **10** (14), 11979–11986.

SON, Y., MARTYS, N.S., HAGEDORN, J.G. & MIGLER, K.B. 2003 Suppression of capillary instability of a polymeric thread via parallel plate confinement. *Macromolecules* **36** (15), 5825–5833.

UCHIYAMA, K., MIGITA, H., OHMURA, R. & MORI, Y.H. 2003 Gas absorption into 'string-of-beads' liquid flow with chemical reaction: application to carbon dioxide separation. *Intl J. Heat Mass Transfer* **46** (3), 457–468.

WAGSTAFF, C., GUBBA, S.R., TRUSCOTT, T., ALGASHGARI, K. & ROBERTS, W.L. 2023 Wire density for a wetted-wire column. *Chem. Engng Sci.* **273**, 118633.

WANG, P., BIAN, R., MENG, Q., LIU, H. & JIANG, L. 2017 Bioinspired dynamic wetting on multiple fibers. *Adv. Mater.* **29** (45), 1703042.

WANG, P., ZHOU, J., XU, B., LU, C., MENG, Q. & LIU, H. 2020 Bioinspired anti-plateau–rayleigh-instability on dual parallel fibers. *Adv. Mater.* **32** (45), 2003453.

ZENG, Z., SADEGHPOUR, A., WARRIER, G. & JU, Y.S. 2017 Experimental study of heat transfer between thin liquid films flowing down a vertical string in the Rayleigh-Plateau instability regime and a counterflowing gas stream. *Intl J. Heat Mass Transfer* **108**, 830–840.

ZHANG, C. & KORNEV, K.G. 2017 Morphological transitions of drop configurations on ribbon-like fibers. *Surf. Innov.* **5** (4), 194–202.